



Toward high capacity and stable manganese-spinel electrode materials: A case study of Ti-substituted system

Sihui Wang^a, Jiong Yang^b, Xiaobiao Wu^a, Yixiao Li^a, Zhengliang Gong^c, Wen Wen^d, Min Lin^c, Jihui Yang^b, Yong Yang^{a,c,*}

^a State Key Laboratory of Physical Chemistry of Solid Surfaces, and Department of Chemistry, College of Chemistry and Chemical Engineering, Xiamen University, Xiamen 361005, PR China

^b Materials Science and Engineering Department, University of Washington, Seattle, WA 98195, USA

^c School of Energy Research, Xiamen University, Xiamen 361005, PR China

^d Shanghai Synchrotron Radiation Facility, Shanghai Institute of Applied Physics, Chinese Academy of Science, Shanghai 201204, PR China

HIGHLIGHTS

- $\text{LiMn}_{2-x}\text{Ti}_x\text{O}_4$ ($x = 1$) fulfill more than 1 Li^+ ion insertion into the spinel structure.
- Ti substitution improves the spinel cycling stability between 2 and 4.8 V.
- Ti substitution can suppress the Jahn–Teller distortion associated with Mn^{3+} ions.
- Ti substitution stabilizes the spinel structure by forming more stable framework.
- The role of Ti substitution is explored by *in situ* XRD and *ab initio* calculations.

ARTICLE INFO

Article history:

Received 17 April 2013

Received in revised form

1 July 2013

Accepted 4 July 2013

Available online 12 July 2013

Keywords:

Lithium manganese titanium oxide

Stable spinel framework

Cycling stability

Lithium-ion battery

ABSTRACT

$\text{LiMn}_{2-x}\text{Ti}_x\text{O}_4$ ($x = 0, 0.5, 1$) cathode materials have been synthesized by a conventional solid state method. The capacity of the as-prepared LiMn_2O_4 , $\text{LiMn}_{1.5}\text{Ti}_{0.5}\text{O}_4$ and LiMnTiO_4 are 252, 198 and 157 mAh g^{-1} , respectively, when charging/discharging over the voltage range of 2.0–4.8 V at a current density of 40 mA g^{-1} , all of which are consistent with more than 1 Li^+ ion insertion into the spinel structure. Compared with the pristine LiMn_2O_4 , Ti-substituted samples exhibit much better cycling stability both at room temperature and 60 °C between 2.0 V and 4.8 V. The underlying mechanism has been investigated by an *in situ* X-ray diffraction technique. The results demonstrate that Ti^{4+} ions can suppress the Jahn–Teller distortion associated with Mn^{3+} , and stabilize the spinel structure during the charging/discharging process. Ti–O bond is stronger than Mn–O bond which yields a more stable spinel framework, i.e., $[\text{Mn}_{2-x}\text{Ti}_x]\text{O}_4$. Moreover, Ti substitution helps lower the concentration of Jahn–Teller Mn^{3+} ions in the spinel structure during discharging process and consequently improves the structural stability. The role of Ti substitution is also confirmed by the *ab initio* calculations.

© 2013 Elsevier B.V. All rights reserved.

1. Introduction

LiMn_2O_4 is a promising cathode material because of its abundance, low cost, being environmentally benign, easy preparation, high working voltage (~ 4 V), and so on [1,2]. In the LiMn_2O_4 structure, Li^+ ions occupy the tetrahedral 8a sites, $\text{Mn}^{3+}/\text{Mn}^{4+}$ ions

are in the octahedral 16d sites, and O^{2-} ions are located in the 32e sites which form a cubic-close-packed array. In a unit cell, there are other empty octahedral sites where small ions, such as Li^+ ions, can be inserted using chemical or electrochemical method [3,4]. Therefore, LiMn_2O_4 material can deliver a theoretical high capacity of 296 mAh g^{-1} (2 Li^+ ions) if Li^+ ions are fully inserted/extracted into/from the spinel structure. Note that when Li^+ ions are inserted, LiMn_2O_4 can also be used as anode material which deliveries initial discharge capacity of 1645 mAh g^{-1} between 3 V and 0 V, with the Mn^{4+} ions reducing to metal Mn [5]. While the structural stability need to be improved to enhance the cycling performance. The rapid development of high energy systems such as advanced portable

* Corresponding author. State Key Laboratory of Physical Chemistry of Solid Surfaces, and Department of Chemistry, College of Chemistry and Chemical Engineering, Xiamen University, Xiamen 361005, PR China. Tel./fax: +86 592 2185753. E-mail address: yyang@xmu.edu.cn (Y. Yang).

electronics and electric vehicles has invigorated the investigation of electrodes with two-electron redox centers [6], which makes LiMn_2O_4 a promising cathode material. However, it is well known that when LiMn_2O_4 is discharged to a low voltage, e.g., 2 V, high spin Mn^{3+} ions may induce severe Jahn–Teller distortion [6–9]. *Ab initio* calculations reveal that the Mn^{3+} ions in LiMn_2O_4 have splitted e_g orbitals and distorted Mn^{3+}O_6 octahedral. The transformation between Mn^{4+}O_6 (with six equivalent Mn–O bonds) and distorted Mn^{3+}O_6 during charge/discharge process will cause mechanical structural instability, leading to poor cycling stability [10–12]. Up to date, this material is only used in the 4 V region with a low capacity of $\sim 120 \text{ mAh g}^{-1}$, far from satisfying the demand of high energy density for electric vehicles. Accordingly, many researchers have focused on improving the structural stability and realizing the high capacity. As we know, the cations applied in substitution are mostly based on monovalent (e.g., Li^+ [13]), divalent (e.g., Ni^{2+} [14], and Mg^{2+} [15]) or trivalent (e.g., Al^{3+} [16], Fe^{3+} [17], Cr^{3+} [18], and Co^{3+} [18]) metal ions which could improve the average oxidation state of Mn ions higher than +3.5 and suppress the Jahn–Teller effect, resulting in better cycling performance compared with pristine LiMn_2O_4 in the 4 V region. However, when the material is used in a wide voltage range (e.g., 2.0–4.8 V) where the Mn^{4+} ions inactive in the 4 V region are further reduced to Mn^{3+} ions, the cycling performance of low-valence-ions-doped materials are not so satisfactory. For example, Lee et al. [19] found that the capacity retention of a $\text{LiAl}_{0.1}\text{Mn}_{1.9}\text{O}_4$ material prepared by using Mn_3O_4 or $\gamma\text{-MnOOH}$ as starting materials were about 30% and 70% after 50 cycles in 2.0–4.3 V range, respectively. When cycled in the voltage range of 2.0–5.0 V, $\text{LiNi}_{0.5}\text{Mn}_{1.5}\text{O}_4$ materials with different transition-metal ion ordering showed large capacity fading with capacity retention between about 45% and 65% [20].

The bonding energy of Ti–O (662 kJ mol^{-1}) is greater than that of Mn–O (402 kJ mol^{-1}), therefore, it is expected that partial substitution of Mn^{4+} by Ti^{4+} could improve the stability of spinel framework. Recently, Lin et al. [21] proved that the cycling performance of 5 V spinel $\text{LiMn}_{1.5}\text{Ni}_{0.5}\text{O}_4$ was greatly improved by Ti substitution in 2.0–4.95 V range owing to the increased structural stability. Our previous work showed some preliminary results about the influence of Ti substitution on the cycling performance of LiMn_2O_4 in a wide voltage range (2.0–4.8 V), where a $\text{LiMn}_{1.2}\text{Ti}_{0.8}\text{O}_4$ electrode delivered a high capacity of $\sim 175 \text{ mAh g}^{-1}$, namely 1.14 Li^+ ions per formula unit, after 50 cycles at 75 mA g^{-1} at 55°C , and showed an improved cycling performance compared with the Ti-free LiMn_2O_4 [22]. However, the average oxidation state of Mn in LiMn_2O_4 is lowered after Ti substitution. Therefore, it is critical to discern: (1) why the materials with large amount of Ti substitution which leads to a lower Mn valence can still exhibit excellent cycling stability, even though more than 1 Li^+ ion is inserted/extracted into/from the spinel unit structure, and (2) how the structure changes during charging and discharging process for $\text{LiMn}_{2-x}\text{Ti}_x\text{O}_4$ materials. In this paper, we compare the electrochemical performance of spinel $\text{LiMn}_{2-x}\text{Ti}_x\text{O}_4$ ($x = 0, 0.5, 1$) materials prepared by a conventional solid state method, apply *ex situ* and *in situ* techniques and conduct *ab initio* calculations to investigate the role of Ti substitution during the electrochemical charge/discharge process.

2. Experimental

Spinel materials $\text{LiMn}_{2-x}\text{Ti}_x\text{O}_4$ ($x = 0, 0.5, 1$) were synthesized by the solid state method. Analytically pure MnCO_3 , Li_2CO_3 and TiO_2 were dispersed in acetone and fully ground by ball milling for 10 h. After drying at 120°C overnight, the mixtures were pressed into pellets and calcined at 800°C for 20 h. 7% excess Li_2CO_3 was added to account for Li evaporative loss during the calcination.

The *ex situ* X-ray diffraction (XRD) patterns were measured using Cu $K\alpha$ radiation ($\lambda = 1.5406 \text{ \AA}$) on a Panalytical X'Pert (Philips, Netherlands) instrument operated at 40 kV and 30 mA between 10° and 90° . Chemical compositions of the samples were determined using inductively coupled plasma/atomic emission spectrometer (ICP-AES) (IRIS Intrepid II XSP, Thermo Electron). The lattice parameters and cation distribution for $\text{LiMn}_{2-x}\text{Ti}_x\text{O}_4$ ($x = 0, 0.5, 1$) compounds were calculated from experimental XRD data and Rietveld refinement software. X-ray photoelectron spectroscopy (XPS) for powder materials and cycled electrodes were measured on a Quantum 2000 ESCA spectrometer (Physical Electronics, USA) at room temperature. *In situ* X-ray diffraction patterns were performed using BL14B1 at the Shanghai Synchrotron Radiation Facility (SSRF) (Shanghai, China) with a wavelength of 1.2398 \AA . The *in situ* cells were designed as previously reported [23], and the detailed description is shown in the Supporting information. The *in situ* XRD data were collected by an image plate detector, which employing a fit2d code to integrate the diffraction ring. And LaB_6 was used for calibration. The current density used in the *in situ* experiment was 40 mA g^{-1} . *Ab initio* calculations using the Vienna *ab initio* simulation package (VASP) [24–26] were performed within the spin-polarized Perdew–Burke–Ernzerhof generalized gradient approximation (PBE-GGA) [27]. The plane-wave cutoff was set to 500 eV, and k -point meshes of $4 \times 4 \times 4$ were used in all the calculations. Structural relaxations were performed with a very accurate $5 \times 10^{-4} \text{ eV \AA}^{-1}$ tolerance of forces. GGA + U was adopted to get accurate total energy and electronic structure, with $U = 4.8 \text{ eV}$ on 3d electronic states of Mn, suggested by Chevrier et al. [10].

CR2025 coin-type cells were fabricated to study the electrochemical performance of these materials. A mixture containing 80 wt% active material, 10 wt% acetylene black, and 10 wt% poly(vinylidene fluoride) binder (PVDF) in *N*-methyl-2-pyrrolidone (NMP) solvent was ground into slurry by ball milling. The resulting slurry was then uniformly coated onto Al current collectors, and dried at 120°C in air overnight prior to use. The cells were assembled in an argon-filled glove box using the as-prepared electrode as cathode, lithium metal as anode, and Celgard 2300 as separator. The electrolyte was 1 M LiPF_6 dissolved in ethylene carbonate (EC)/dimethyl carbonate (DMC) with a volume ratio of 1:1. Galvanostatic charge/discharge tests were carried out at different current densities at room temperature and 60°C between 2.0 and 4.8 V (vs. Li/Li^+) on Land CT 2001A battery testers. Cycled batteries were unassembled in the glove box, and the cathode electrodes were thoroughly washed by dimethyl carbonate (DMC) solvent before *ex situ* XRD and XPS measurements.

3. Results and discussion

Fig. 1 shows the X-ray diffraction patterns of Ti substituted $\text{LiMn}_{2-x}\text{Ti}_x\text{O}_4$ ($x = 0, 0.5, 1$) powders. All diffraction peaks can be indexed to the cubic spinel structure with a space group of $Fd\bar{3}m$, in accordance with previous reports [18,22,28,29]. Substituted Ti ions are in the +4 oxidation state which is confirmed by XPS results in Fig. S1(a) in the Supporting information. No impurity phases arise with the increasing Ti content, and the diffraction peaks continuously shift toward lower diffraction angles due to the larger radius of Ti^{4+} (0.61 \AA) than that of Mn^{4+} (0.53 \AA) ions, indicating that Ti^{4+} ions are successfully incorporated into the spinel Mn^{4+} sublattice. 220 diffraction peak is obviously observed in $\text{LiMn}_{1.5}\text{Ti}_{0.5}\text{O}_4$ and LiMnTiO_4 samples, and its intensity increases with increasing Ti content, which suggests that Ti substitution induces some heavy atoms into 8a sites, since the appearance of 220 diffraction peak represents heavy atoms occupation in the tetrahedral 8a sites in spinel structure [9,16,30–32]. Ti [33] and Mn [13,28,29] atoms have been considered to be able to replace some Li in the 8a sites.

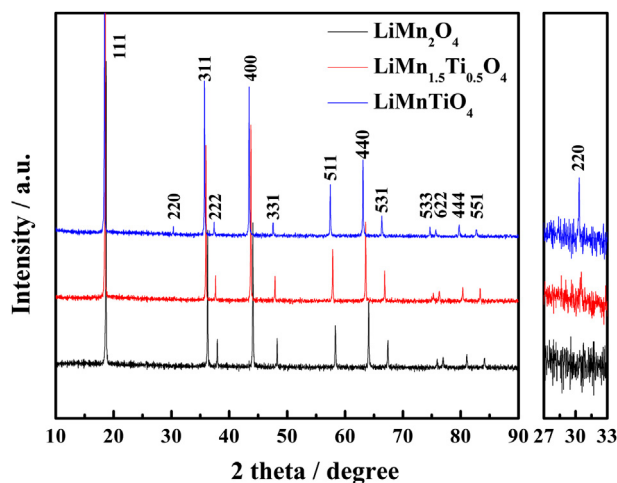


Fig. 1. XRD patterns of as-prepared $\text{LiMn}_{2-x}\text{Ti}_x\text{O}_4$ ($x = 0, 0.5, 1$) materials ($\lambda = 1.5406 \text{ \AA}$).

However, Petrov et al. [29] and Krins et al. [28] proved that Mn^{2+} ions, rather than Ti^{4+} ions, should be the more suitable ones that randomly occupy the tetrahedral 8a sites in the spinel structure. Therefore, the more Mn^{2+} ions entering the 8a sites with increasing Ti content in the structure, the greater 220 diffraction peak intensity on its XRD pattern is. Based on $\text{Li}^+/\text{Mn}^{2+}$ cation mixing, the cation distribution for $\text{LiMn}_{2-x}\text{Ti}_x\text{O}_4$ ($x = 0, 0.5, 1$) compounds were calculated from experimental XRD data and Rietveld refinement software with the data shown in Table 1. Evidently, more and more Mn^{2+} ions occupy the 8a site with the increase of Ti content. However, $\text{Li}^+/\text{Mn}^{2+}$ mixing can restrict Li^+ ions diffusion, which may deteriorate the rate capability. The results of ICP-AES elemental analysis are displayed in Table 2, where the amount of Mn is normalized to the stoichiometry of 2, 1.5 and 1, respectively, for LiMn_2O_4 , $\text{LiMn}_{1.5}\text{Ti}_{0.5}\text{O}_4$ and LiMnTiO_4 . The ICP-AES results confirm that all actual compositions of the as-prepared samples are in good agreement with their nominal compositions although their Li contents are slightly higher owing to the excess Li_2CO_3 used in preparation. Hereafter, we use the nominal formula of LiMn_2O_4 , $\text{LiMn}_{1.5}\text{Ti}_{0.5}\text{O}_4$ and LiMnTiO_4 in the whole paper for convenience.

Fig. 2(a) shows the 1st charge/discharge profiles of $\text{LiMn}_{2-x}\text{Ti}_x\text{O}_4$ ($x = 0, 0.5, 1$) electrodes over the voltage range of 2.0–4.8 V at 40 mA g^{-1} at room temperature. LiMn_2O_4 electrode shows two charge plateaus at around 4.0 V and 4.15 V which are characteristic of Li^+ ions extracted from tetrahedral 8a sites, leading to the gradual transformation from pristine LiMn_2O_4 to $\lambda\text{-MnO}_2$ [34]. During discharging process, two corresponding voltage plateaus appear at around 3.9 V and 4.1 V, followed by a long plateau near 2.8 V which corresponds to a two-phase reaction forming

Table 1
Cation distribution for $\text{LiMn}_{2-x}\text{Ti}_x\text{O}_4$ ($x = 0, 0.5, 1$) compounds calculated from experimental XRD data and Rietveld refinement software.

	Site	Atom	LiMn_2O_4	$\text{LiMn}_{1.5}\text{Ti}_{0.5}\text{O}_4$	LiMnTiO_4
SOF ^a	8a	Li	0.989(2)	0.949(2)	0.845(2)
		Mn	0.011(2)	0.051(2)	0.155(2)
	16d	Li	0.005(2)	0.026(3)	0.078(3)
		Mn	0.995(2)	0.724(3)	0.422(3)
		Ti	0.000	0.250	0.500

^a SOF represents site occupancy factors.

Table 2
ICP-AES elemental analysis and intensity ratios of tetragonal 103 (103_T)/cubic 111 (111_C) diffraction peaks.

Theoretical stoichiometry	Measured stoichiometry from ICP-AES			I_{103T}/I_{111C}^b
	Li	Mn	Ti	
LiMn_2O_4	1.02	2.00	0	0.131
$\text{LiMn}_{1.5}\text{Ti}_{0.5}\text{O}_4$	1.02	1.50	0.51	0.049
LiMnTiO_4	1.03	1.00	0.99	0

^b T and C represent tetragonal and cubic phase, respectively.

tetragonal $\text{Li}_2\text{Mn}_2\text{O}_4$ phase when extra Li^+ ions are inserted into the octahedral 16c sites [8,19]. The discharge capacity of LiMn_2O_4 is 252 mAh g^{-1} , equivalent to 1.70 Li^+ ions intercalation. After Ti substitution, the plateaus related to Li^+ ions extraction/insertion from/into the tetrahedral 8a sites become less evident. The discharge capacities of $\text{LiMn}_{1.5}\text{Ti}_{0.5}\text{O}_4$ and LiMnTiO_4 are 198 mAh g^{-1} (1.31 Li^+ ions intercalation) and 157 mAh g^{-1} (1.02 Li^+ ions intercalation), respectively. There are three main reasons for the different capacities between pristine LiMn_2O_4 and Ti-substituted ones. Firstly, the Ti substitution induces more Li/Mn cation mixing in the structure confirmed by the XRD result in Fig. 1

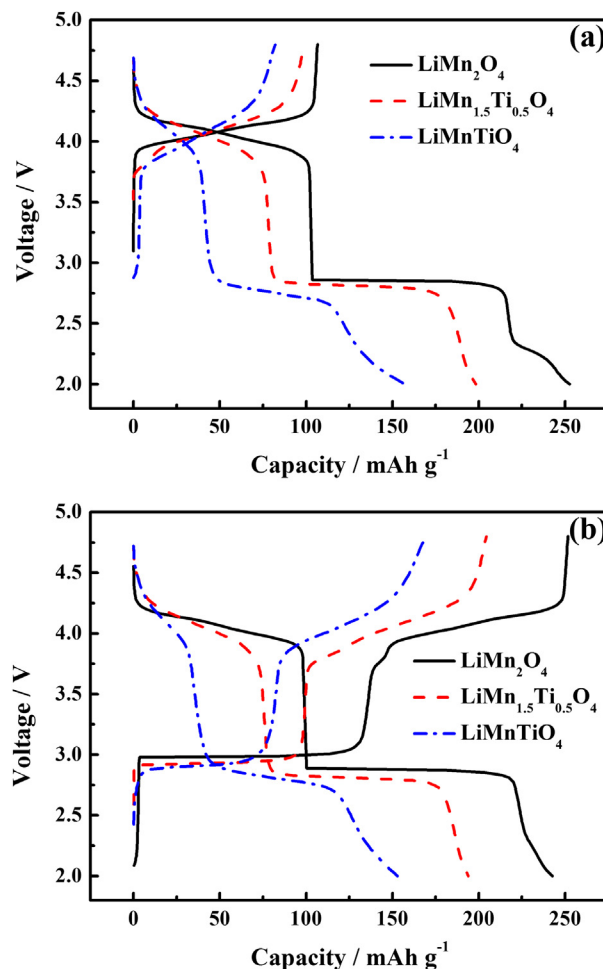


Fig. 2. The (a) 1st and (b) 2nd charge/discharge profiles of $\text{LiMn}_{2-x}\text{Ti}_x\text{O}_4$ ($x = 0, 0.5, 1$) electrodes over the voltage range of 2.0–4.8 V at a current density of 40 mA g^{-1} at room temperature.

and Rietveld refinement data in Table 1. Li^+ ions migrate through the path of 8a–16c–8a in the spinel structure, therefore, Li^+ ions in the 16d sites cannot be deintercalated during charging, and the 8a sites occupied by Mn^{2+} ions cannot accommodate Li^+ ions during discharging, leading to the reduced capacity after Ti substitution. Secondly, the cation mixing and doping cause some local structure distortion [35] and enlarged polarization, which are unfavorable for Li^+ diffusion. Finally, capacity of $\text{LiMn}_{1.5}\text{Ti}_{0.5}\text{O}_4$ and LiMnTiO_4 materials may be compromised partially on account of the slightly larger particle size and more serious agglomeration compared with Ti-free LiMn_2O_4 (The SEM images are shown in Fig S2 in the Supporting information). Due to the above issues, the first charge/discharge capacity of LiMn_2O_4 is higher than the other two Ti-substituted materials.

As can be seen in Fig. 2(a), LiMnTiO_4 electrode shows a charge capacity of 81 mAh g^{-1} and Mn^{4+} ions caused by charging should all be reduced to Mn^{3+} ions at the identical discharge capacity. Therefore, there must be some other ions participating in the redox reaction to obtain the extra discharge capacity. Ti^{4+} ions are electrochemical inactive in 2.0–4.8 V range [36,37] which is also supported by the XPS data in Fig. S1(a) (Supporting information), so some Mn^{3+} ions should be reduced to Mn^{2+} ions in the 3 V region. The Mn 3s XPS results shown in Fig. S1(b) (Supporting information) prove the presence of Mn^{2+} ions which confirm our speculation. Namely, LiMnTiO_4 sample shows different reaction mechanism compared with LiMn_2O_4 in the 3 V region. In addition, Fig. S1(c) shows that some Mn^{3+} ions in $\text{LiMn}_{1.5}\text{Ti}_{0.5}\text{O}_4$ are also reduced to Mn^{2+} as that happens in LiMnTiO_4 , while the amount of reduced Mn^{3+} ions is rather small. The 2nd charge/discharge profiles of $\text{LiMn}_{2-x}\text{Ti}_x\text{O}_4$ are shown in Fig. 2(b). All the electrodes show distinct plateaus in 3 V and 4 V regions for both charging and discharging. The discharge profiles of Ti-substituted samples are well retained in the 2nd cycle, while the discharge plateau of LiMn_2O_4 at about 2.3 V nearly disappears. The reason for this phenomenon is not clear at this stage.

Cycling performance is a very important property for lithium-ion batteries. However, LiMn_2O_4 spinel material typically exhibits rapid capacity fading especially at elevated temperatures [31,38]. Cycling performance of $\text{LiMn}_{2-x}\text{Ti}_x\text{O}_4$ at room temperature and 60°C with current density of 40 and 200 mA g^{-1} are shown in Fig. 3. The capacity of LiMn_2O_4 rapidly decreases during cycling at 40 mA g^{-1} current density in the voltage range of 2.0–4.8 V at room temperature, as shown in Fig. 3(a). The capacity for LiMn_2O_4 is only 84 mAh g^{-1} with capacity retention of 33% after 80 cycles. In comparison, $\text{LiMn}_{1.5}\text{Ti}_{0.5}\text{O}_4$ and LiMnTiO_4 deliver the capacities of 155 and 139 mAh g^{-1} , with the capacity retention of 76% and 83%, respectively, after 80 cycles. In particular, $\text{LiMn}_{1.5}\text{Ti}_{0.5}\text{O}_4$ sample shows excellent cycling performance with more than 1 Li^+ ion insertion/extraction into/from the spinel structure. Fig. 3(b) shows the cycling performance with the current density of 200 mA g^{-1} at 60°C , which indicates that LiMn_2O_4 exhibits much severe capacity fading compared with Ti-substituted samples. In a word, the capacity fading of $\text{LiMn}_{1.5}\text{Ti}_{0.5}\text{O}_4$ and LiMnTiO_4 samples are greatly alleviated in contrast with that of LiMn_2O_4 sample both at room temperature and at 60°C .

We employed the *in situ* XRD technique to obtain information of structural changes during charging and discharging process. *In situ* X-ray diffraction patterns for LiMn_2O_4 , $\text{LiMn}_{1.5}\text{Ti}_{0.5}\text{O}_4$ and LiMnTiO_4 electrodes during the 1st cycle are illustrated in Fig. 4, and the *in situ* XRD patterns for the 111 diffraction peaks of cubic phase are shown in Fig. S3 in the Supporting information. It can be seen that during charging accompanied by Li^+ ions extracting from the spinel structure, diffraction peaks of the cubic phase shift to higher diffraction angles. On the contrary, when Li^+ ions are inserted back into the structure upon discharging, the diffraction

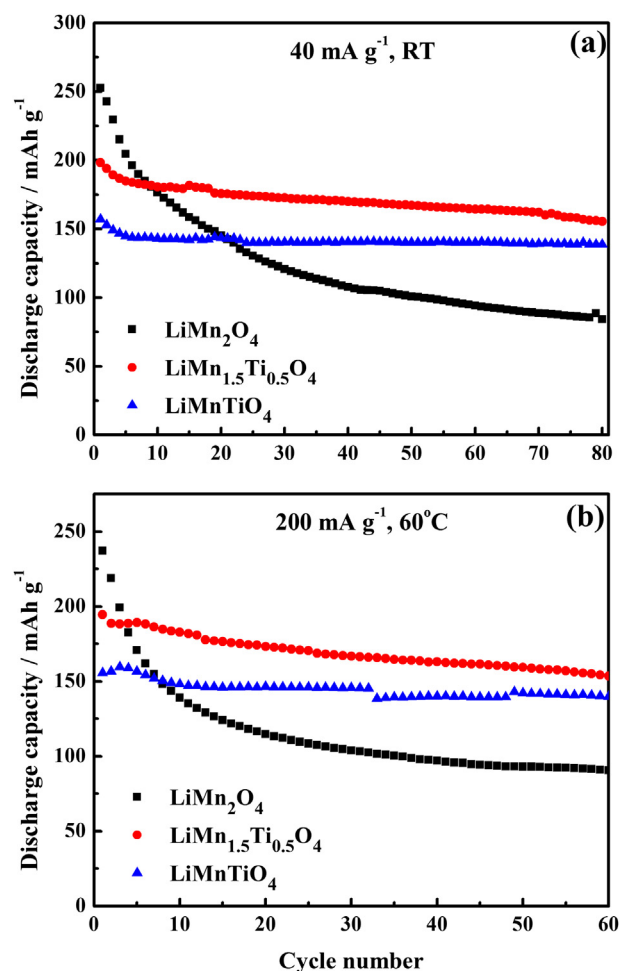


Fig. 3. Cycling performance of $\text{LiMn}_{2-x}\text{Ti}_x\text{O}_4$ ($x = 0, 0.5, 1$) at a current density of (a) 40 mA g^{-1} at room temperature (RT) and (b) 200 mA g^{-1} at 60°C .

peaks shift back toward the lower angles. The peak shifting during charging and discharging process indicates the lattice shrinking and expanding, respectively. Cubic phase transformation typically reported for LiMn_2O_4 or its derivatives in the 4 V region [39–41] does not occur for our $\text{LiMn}_{2-x}\text{Ti}_x\text{O}_4$ ($x = 0, 0.5, 1$) electrodes. This might be ascribed to the different experimental conditions, such as the relatively high current density (40 mA g^{-1}) we applied. The detailed changes of lattice parameter will be discussed later. During the initial discharging, the electrode materials were all cubic symmetry. New diffraction peaks arise when LiMn_2O_4 and $\text{LiMn}_{1.5}\text{Ti}_{0.5}\text{O}_4$ electrodes were discharged to the $\sim 2.8 \text{ V}$ plateau at the discharge capacities of 137 and 119 mAh g^{-1} in Fig. 4(a) and (c) respectively. The newly developed peaks are indexed to a tetragonal symmetry structure, whose contents gradually increase upon discharging as evidenced by progressive development of these peaks. By contrast, LiMnTiO_4 electrode does not show these new peaks in the whole discharging process (Fig. 4(e)). It is generally believed that the severe capacity fading of LiMn_2O_4 electrode is mainly attributed to the formation of tetragonal phase which greatly increases the c/a ratio (16%) in the unit cell. It is hard for LiMn_2O_4 to maintain the structure integrity, thus the capacity decreases rapidly. Though Ti^{4+} substitution may decrease the average valence of Mn lower than +3.5, it can form more stable TiO_6 octahedron than MnO_6 because of the larger bonding energy of Ti–O than that of Mn–O. Therefore, instead of $[\text{Mn}_2]\text{O}_4$, the

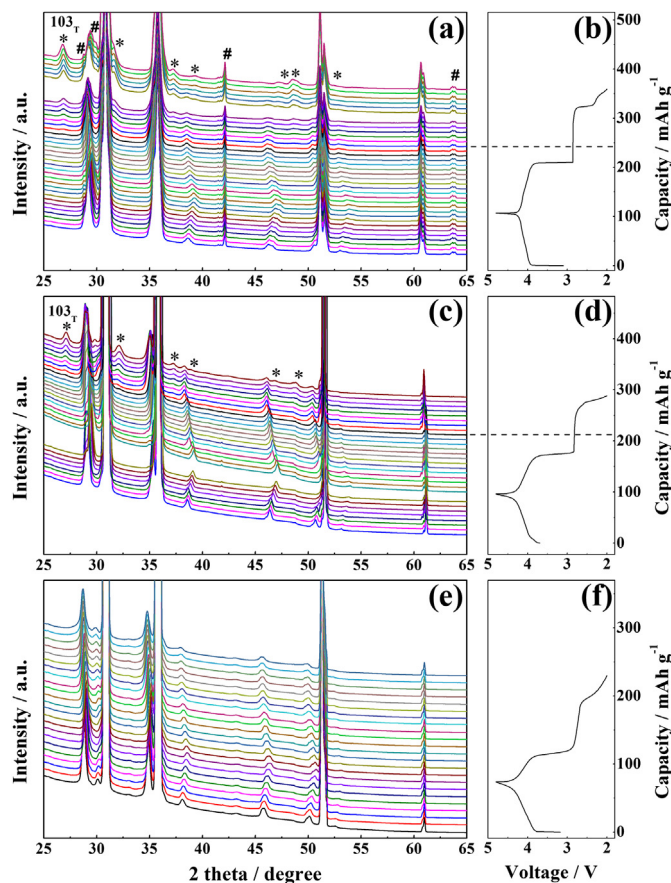


Fig. 4. *In situ* XRD patterns for LiMn₂O₄ ((a), (b)), LiMn_{1.5}Ti_{0.5}O₄ ((c), (d)), and LiMnTiO₄ ((e), (f)) electrodes during the 1st cycle. T in the figure represents the tetragonal symmetry structure. Peaks labeled with * and # are signal from the tetragonal phase and background, respectively ($\lambda = 1.2398 \text{ \AA}$).

more stable [Mn_{2-x}Ti_x]O₄ spinel framework improves the structural stability during the deep charging/discharging process. Meanwhile, Mn³⁺ ions were partially reduced to Mn²⁺ ions in LiMnTiO₄ in the 3 V region, as discussed in Fig. 2, leading to the decrease of Jahn–Teller Mn³⁺ ions, which also helps to improve the structural stability. At elevated temperatures, the dissolution of Mn²⁺ ions is accelerated, which may lead to faster structure collapse and severe capacity loss. While the dissolution of Mn²⁺ ions can be suppressed by Ti substitution [21]. With more stable framework, LiMn_{1.5}Ti_{0.5}O₄ and LiMnTiO₄ electrodes still show excellent cycling stability as illustrated in Fig. 3(b). Therefore, the stabilized structure contributes substantially to the cycling stability after Ti substitution. The intensity ratios of tetragonal 103 (103_T) and cubic 111 (111_C) diffraction peaks, I_{103T}/I_{111C} , for these electrodes discharged to 2 V are listed in Table 2. It is clear that the intensity ratio reduces from 0.131 to 0.049 and finally to 0 after Ti substitution. Assuming that the intensity ratio between tetragonal 103 and cubic 111 diffraction peaks are simply indicative of the mole ratio between the tetragonal and cubic phases, all these demonstrate that Ti⁴⁺ substitution for partial Mn⁴⁺ ions does suppress the Jahn–Teller distortion in the 3 V region, but only with high Ti⁴⁺ concentrations. For example, in our design, the critical value should be in the range of $0.5 < x \leq 1$. It is also true that Ti substitution greatly improves the cycling performance at the expense of discharge capacity, so the content of Ti should be optimized to obtain overall better properties.

Fig. 5 shows the *in situ* X-ray diffraction patterns for LiMn₂O₄, LiMn_{1.5}Ti_{0.5}O₄ and LiMnTiO₄ electrodes during the 2nd cycle. The intensity of diffraction peaks associated with the tetragonal phase gradually decrease during the 2nd charging process, and these peaks completely vanish at 4 V (Fig. 5(b) and (d)) which is consistent with the previous report [40]. LiMnTiO₄ electrode does not show any evidence of the tetragonal phase even in the deeply discharged state of the 2nd cycle. Fig. S4 in the Supporting information depicts the *ex situ* X-ray diffraction patterns of the fresh and cycled LiMnTiO₄ electrodes. The results demonstrate that LiMnTiO₄ only has lattice shrinking and expanding rather than cubic to tetragonal phase transformation during the electrochemical cycling. The *in situ* and *ex situ* XRD results indicate that high concentration of Ti substitution can suppress the Jahn–Teller distortion, resulting in improved structural integrity which can improve the cycling performance.

Fig. 6 shows the calculated lattice parameters of spinel and tetragonal phases for LiMn_{2-x}Ti_xO₄ during the 1st cycle. According to the relationship of parameters between cubic and tetragonal phases, which are $a_T = a_C/\sqrt{2}$ and $c_T = a_C$, the cubic phase parameters were converted into those of the tetragonal phase, where T and C represent tetragonal and cubic phase, respectively. Lattice parameter and volume variation of a_T , c_T and V_T at 4.8 V and 2 V compared with those of the fresh electrodes are summarized in Table 3. The lattice parameters of LiMn₂O₄ electrode material are $a_T = 5.7839 \text{ \AA}$ and $c_T = 8.1797 \text{ \AA}$ at the open circuit potential, and they decrease to 5.6843 and 8.0388 \AA , respectively, at the fully charged state (4.8 V), both with a 1.72% reduction during the 1st charge. After the 1st charging process, the lattice parameters

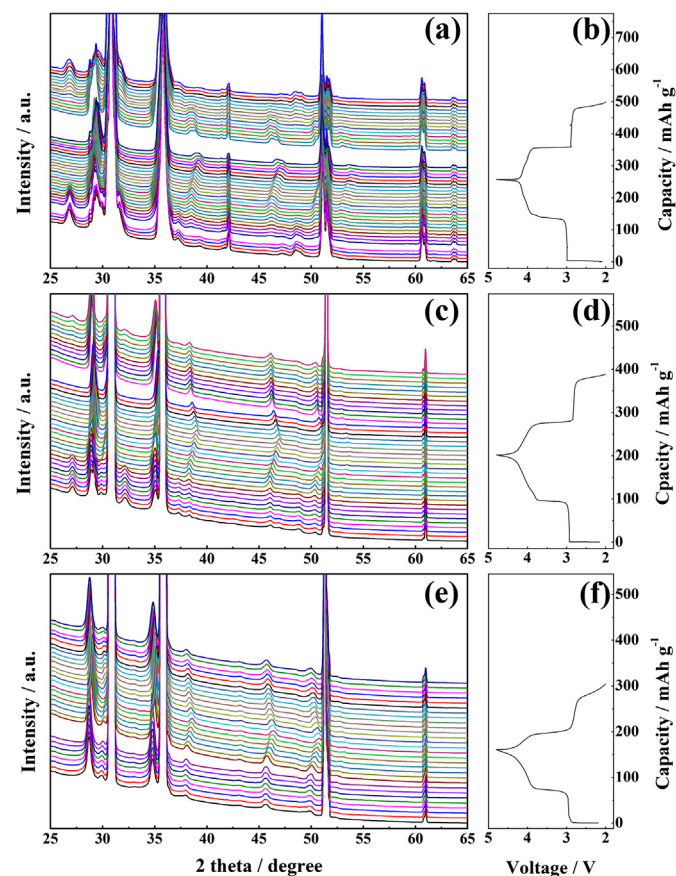


Fig. 5. *In situ* X-ray diffraction patterns for LiMn₂O₄ ((a), (b)), LiMn_{1.5}Ti_{0.5}O₄ ((c), (d)), and LiMnTiO₄ ((e), (f)) electrodes during the 2nd cycle ($\lambda = 1.2398 \text{ \AA}$).

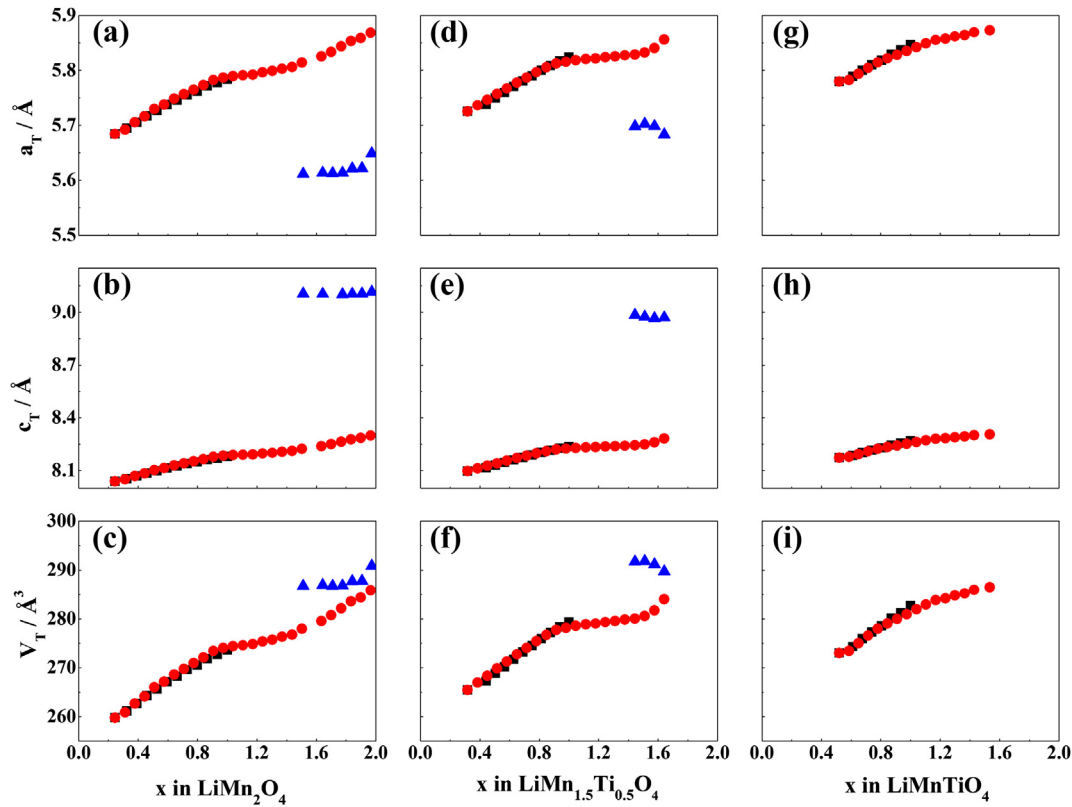


Fig. 6. Lattice parameters of LiMn_2O_4 (a, b, c), $\text{LiMn}_{1.5}\text{Ti}_{0.5}\text{O}_4$ (d, e, f), and LiMnTiO_4 (g, h, i) electrodes during the 1st cycle. Symbols “■”, “●” and “▲” represent cubic phase during charging, cubic phase during discharging, and tetragonal phase during discharging, respectively.

change from $a_T = 5.8240 \text{ Å}$, $c_T = 8.2364 \text{ Å}$ to $a_T = 5.7255 \text{ Å}$, $c_T = 8.09714 \text{ Å}$ and from $a_T = 5.8473 \text{ Å}$, $c_T = 8.2693 \text{ Å}$ to $a_T = 5.7798 \text{ Å}$, $c_T = 8.1738 \text{ Å}$ for LiMn_2O_4 , $\text{LiMn}_{1.5}\text{Ti}_{0.5}\text{O}_4$ and LiMnTiO_4 , with the lattice parameters reduction of 1.69% and 1.15%, respectively. After the 1st discharging process, the cubic lattice parameters expand by 1.47%, 0.55%, and 0.44% for LiMn_2O_4 , $\text{LiMn}_{1.5}\text{Ti}_{0.5}\text{O}_4$, and LiMnTiO_4 electrodes, respectively, compared with the values at their open circuit potentials. It can be seen in Table 3 that the volume expansion of cubic phase increases in the order of LiMnTiO_4 (1.32%) < $\text{LiMn}_{1.5}\text{Ti}_{0.5}\text{O}_4$ (1.67%) < LiMn_2O_4 (4.46%) at the end of discharge. At the same time, the formed tetragonal phase in LiMn_2O_4 and $\text{LiMn}_{1.5}\text{Ti}_{0.5}\text{O}_4$ electrodes induces significant changes in lattice parameter which destroys the spinel structure integrity. The lattice structure does undergo more drastic change for pristine LiMn_2O_4 electrode material, and Ti substitution mitigates this change. The large lattice parameter change leads to large volume change during cycling, which may cause structural degradation and introduce loss of contact between particles, leading to large capacity loss and inferior cycling property. These results are in agreement with cycling stability increase in the order of LiMn_2O_4 < $\text{LiMn}_{1.5}\text{Ti}_{0.5}\text{O}_4$ < LiMnTiO_4 .

Ab initio calculations were carried out to further rationalize the role of Ti substitution in spinel structure. In the case of LiMn_2O_4 , there are two kinds of Mn ions (equal amount), distinguished by their bond lengths with adjacent O atoms. One (Mn ion) has two different Mn–O bonds (1.96 Å and 2.10 Å), while the other has six identical Mn–O bonds (1.95 Å). Fig. 7(a) shows the total density of states (DOS) of both spin up and spin down, as well as the projected DOS on each type of Mn ions. Zero energy point is the Fermi level. The electronic configurations and therefore, valences of Mn ions are determined by their net spin integrations, which can be taken as the integrations of spin up projected DOS minus those of spin down [42]. Based on the projected DOS in Fig. 7(a), the net spin values are 4.0 for the Mn ions with two different Mn–O bonds, and 3.3 for the Mn ions with six identical Mn–O bonds. The former corresponds to an electronic configuration $t_{2g}^3 e_g^1$ (Mn^{3+}) and latter to t_{2g}^3 (Mn^{4+}); with theoretical net spin being 4.0 and 3.0, respectively. Our calculations are consistent with 50% each of Mn^{4+} and Mn^{3+} in LiMn_2O_4 . Mn^{3+} ions show splitted and half-occupied e_g orbitals (Fig. 7(a)), typical for the Jahn–Teller effect. Their nonequivalent Mn–O bonds are the underlying reason for phase transformation to the tetragonal structure associated with

Table 3

Lattice parameter variation of cubic phase charged to 4.8 V ($C_{4.8V}$), cubic phase discharged to 2.0 V ($C_{2.0V}$), and tetragonal phase discharged to 2.0 V ($T_{2.0V}$) compared with those of the fresh electrodes.

Variation/%	LiMn_2O_4			$\text{LiMn}_{1.5}\text{Ti}_{0.5}\text{O}_4$			LiMnTiO_4		
	$C_{4.8V}$	$C_{2.0V}$	$T_{2.0V}$	$C_{4.8V}$	$C_{2.0V}$	$T_{2.0V}$	$C_{4.8V}$	$C_{2.0V}$	$T_{2.0V}$
a_T	−1.72	+1.47	−2.34	−1.69	+0.55	−2.42	−1.15	+0.44	None
c_T	−1.72	+1.47	+11.43	−1.69	+0.55	+8.91	−1.15	+0.44	None
V_T	−5.08	+4.46	+6.29	−5.00	+1.67	+3.70	−3.42	+1.32	None

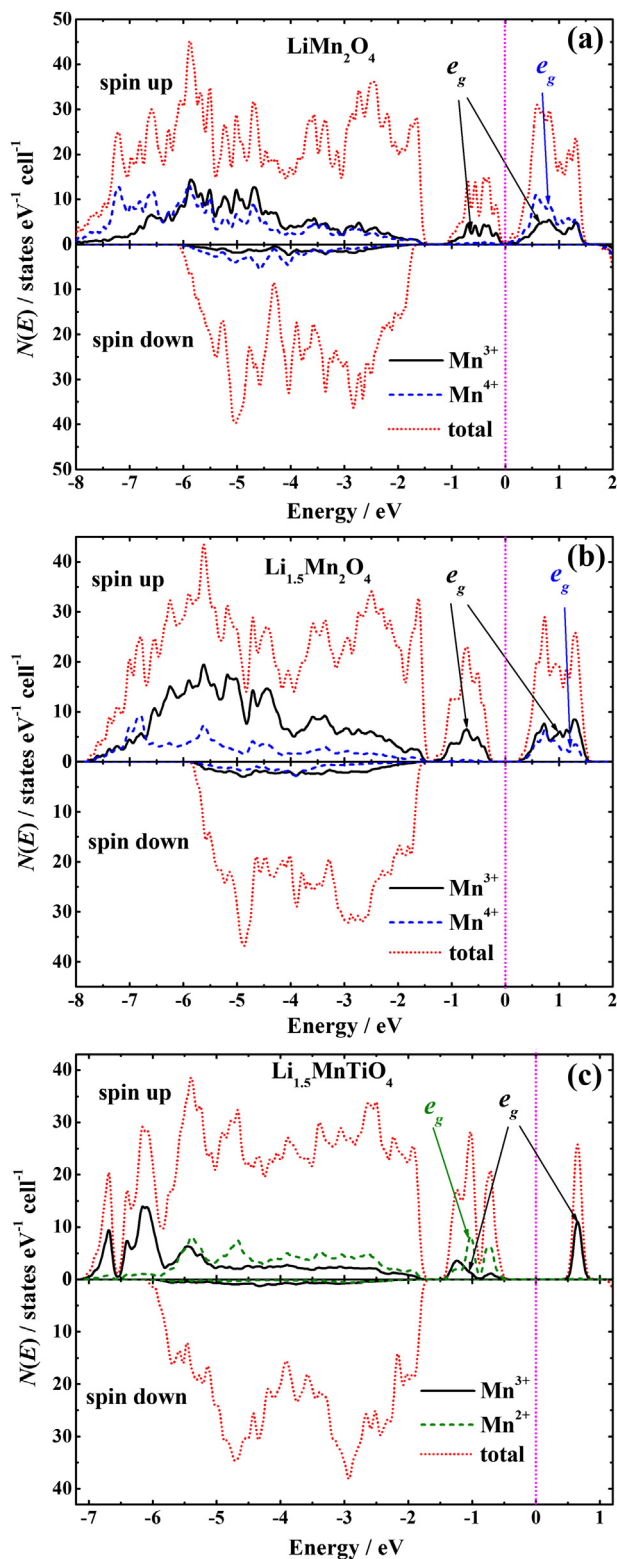


Fig. 7. Total density of states (DOS) and projected DOS for Mn ions in (a) LiMn_2O_4 , (b) $\text{Li}_{1.5}\text{Mn}_2\text{O}_4$, and (c) $\text{Li}_{1.5}\text{MnTiO}_4$. Zero points are the Fermi levels. e_g orbitals of Mn ions in spin up are labeled.

poor cycling stability. Our DOS calculations for LiMn_2O_4 are close to those carried by Xu et al. [11].

For LiMnTiO_4 , based on the same methodology, it is found that all Mn ions possess the electronic configurations close to $t_{2g}^3e_g^1$ (net

spin close to 3.3), i.e., Mn^{3+} , and all Ti ions are Ti^{4+} . Ti substitution does not lower the amount of Mn^{3+} ions on octahedral 16d sites even in $\text{Li}_x\text{MnTiO}_4$ when $x \leq 1$; however, it enhances mechanical properties. Our calculations show that the bulk modulus for LiMnTiO_4 is 105 GPa, which is 17% larger than that for LiMn_2O_4 (90 GPa). This result demonstrates that Ti–O has stronger chemical bonding, and leads to improved stability found in Ti-substituted spinel structure.

When discharged to lower voltages, i.e., $x > 1$ in $\text{Li}_x\text{Mn}_2\text{O}_4$ or $\text{Li}_x\text{MnTiO}_4$, the Fermi levels would move to higher energy, and therefore Li ion insertion further reduces transition metal ions. Fig. 7(b) and (c) presents the total DOS and projected DOS of Mn ions for $\text{Li}_{1.5}\text{Mn}_2\text{O}_4$ and $\text{Li}_{1.5}\text{MnTiO}_4$, respectively. As LiMn_2O_4 is discharged to $\text{Li}_{1.5}\text{Mn}_2\text{O}_4$ (shown in Fig. 7(b)), there would be increasingly more Mn^{3+} ions than Mn^{4+} , indicative of reduction of Mn^{4+} to Mn^{3+} . On the other hand, half of the Mn ions in $\text{Li}_{1.5}\text{MnTiO}_4$ show net spin of 4.7, indicating an electronic configuration $t_{2g}^3e_g^2$, i.e., Mn^{2+} (theoretical net spin = 5.0). Mn^{2+} ions have all the e_g orbitals in spin up fully occupied (Fig. 7(c)) and six equivalent Mn–O bonds. Thus, in contrast with $\text{Li}_x\text{Mn}_2\text{O}_4$, the amount of Mn^{3+} is lowered in $\text{Li}_x\text{MnTiO}_4$ when $x > 1$. Ti-substitution will help to reduce the structural instability associated with Mn^{3+} . In summary, based on our calculations, Ti-substitution improves the stability of spinel structure in two ways: enhanced mechanical properties due to strong Ti–O bonds, and lower amount of Mn^{3+} when over-discharged, both of which are consistent with our experiments.

Rate capability of LiMn_2O_4 , $\text{LiMn}_{1.5}\text{Ti}_{0.5}\text{O}_4$, and LiMnTiO_4 electrodes were investigated at different current densities (40, 100, 200, 400 and 1000 mA g^{-1}) over the voltage range of 2.0–4.8 V at room temperature, and the results are shown in Fig. 8(a)–(c). The discharge capacities of LiMn_2O_4 , $\text{LiMn}_{1.5}\text{Ti}_{0.5}\text{O}_4$, and LiMnTiO_4 electrodes are 252, 198 and 157 mAh g^{-1} , respectively, at 40 mA g^{-1} rate. When the current density increases to 1000 mA g^{-1} , the discharge capacities of LiMn_2O_4 , $\text{LiMn}_{1.5}\text{Ti}_{0.5}\text{O}_4$, and LiMnTiO_4 electrodes are 151, 168 and 88 mAh g^{-1} , respectively. The normalized discharge capacities are illustrated in Fig. 8(d). Obviously, $\text{LiMn}_{1.5}\text{Ti}_{0.5}\text{O}_4$ electrode possesses the best rate capability, and the rate capability of LiMn_2O_4 and LiMnTiO_4 were quite similar. What about the rate performance of these electrodes without severe Jahn–Teller distortion? Most of the published data about spinel materials were focused on the properties above 3 V, so we also investigated the rate capability with the cut-off voltage of 3.0 V, and the corresponding results are shown in Fig. 8(e). In Fig. 8(e), LiMn_2O_4 electrode exhibits superior rate capability than $\text{LiMn}_{1.5}\text{Ti}_{0.5}\text{O}_4$ and LiMnTiO_4 electrodes. As we know, LiMn_2O_4 spinel has 3 D interstitial space which can facilitate Li^+ ions diffusion through the path of $8a-16c-8a$ in the spinel without restriction [7,9], so the rate capability can be quite good in the 4 V region. Ti substitution in spinel structure increases the site exchange of Li^+ and Mn^{2+} ions, as discussed in Fig. 1 and Table 1, generating a barrier against Li^+ ions migration in the substituted spinel structure, so the rate capability of $\text{LiMn}_{1.5}\text{Ti}_{0.5}\text{O}_4$ and LiMnTiO_4 decreases. In addition, phase transformation from cubic to tetragonal phase caused by Jahn–Teller effect induces large distortion in the structure which can seriously affect electrode properties. Though Li^+ can migrate faster in pristine LiMn_2O_4 compared with $\text{LiMn}_{1.5}\text{Ti}_{0.5}\text{O}_4$ and LiMnTiO_4 samples, LiMn_2O_4 electrode still possesses poor rate performance over the wide voltage range of 2.0–4.8 V because of the severe Jahn–Teller distortion. $\text{LiMn}_{1.5}\text{Ti}_{0.5}\text{O}_4$ electrode with moderate $\text{Li}^+/\text{Mn}^{2+}$ mixing and alleviated Jahn–Teller distortion shows the best rate performance. In the LiMnTiO_4 electrode, the severe site exchange of Li^+ and Mn^{2+} ions destroys its rate capability over the 2.0–4.8 V range, even though Jahn–Teller effect is completely suppressed.

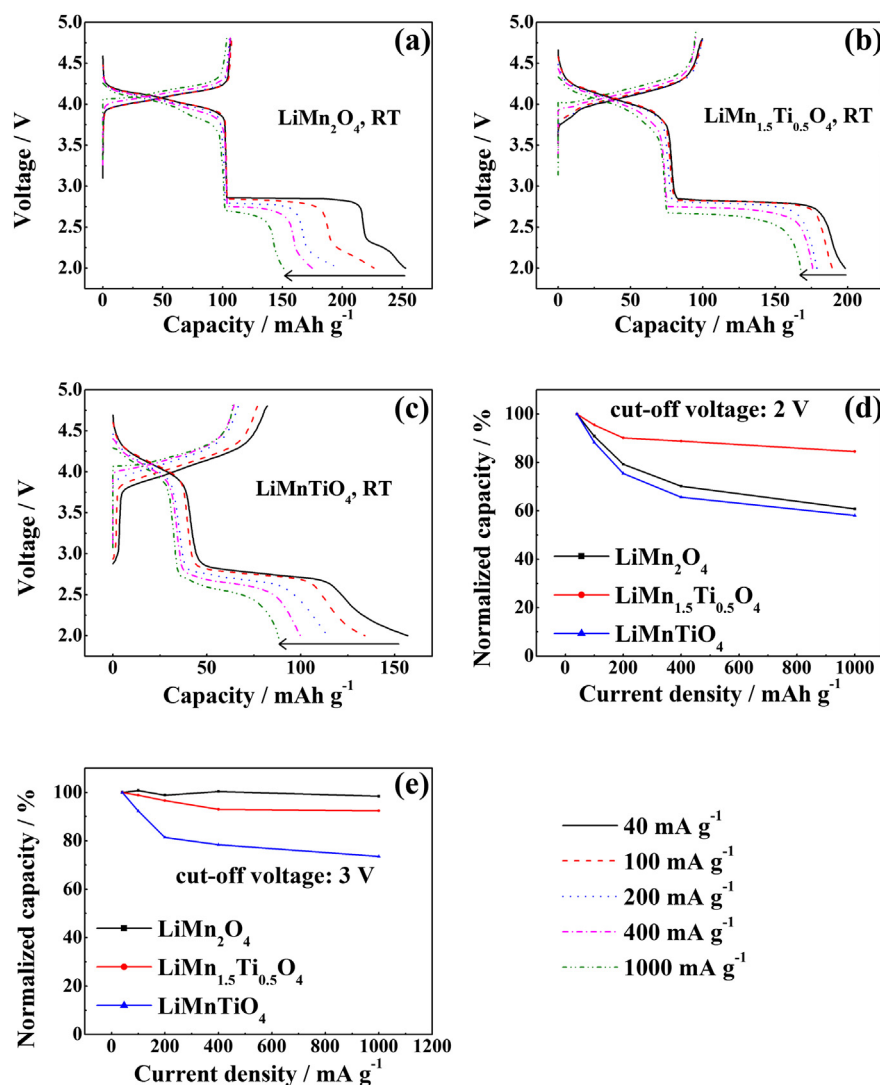


Fig. 8. Rate capability of (a) LiMn_2O_4 , (b) $\text{LiMn}_{1.5}\text{Ti}_{0.5}\text{O}_4$, and (c) LiMnTiO_4 at room temperature. Normalized discharge capacity with cut-off voltage of 3 V and 2 V are illustrated in (d) and (e), respectively.

4. Conclusions

Compared with the pristine LiMn_2O_4 , Ti-substituted samples show significantly improved cycling stability. For example, after 80 cycles, $\text{LiMn}_{1.5}\text{Ti}_{0.5}\text{O}_4$ and LiMnTiO_4 electrodes still deliver capacities of 155 and 139 mAh g^{-1} , with the capacity retention of 76% and 83%, respectively, at the current density of 40 mA g^{-1} . $\text{LiMn}_{1.5}\text{Ti}_{0.5}\text{O}_4$ electrode shows rather excellent cycling performance with more than 1 Li^+ ion insertion/extraction into/from the spinel structure. The mechanism of enhanced cycling performance by Ti substitution was investigated upon cycling in a wide voltage range of 2.0–4.8 V. *In situ* X-ray diffraction patterns confirm that sufficient Ti content in the material can completely suppress Jahn–Teller distortion. Ti substitution can stabilize the spinel structure via forming a more stable $[\text{Mn}_{2-x}\text{Ti}_x]\text{O}_4$ framework, which alleviates the Jahn–Teller distortion in the 3 V region and improves the cycling performance in a wide voltage range. Meanwhile, Ti substitution reduces some Mn^{3+} to Mn^{2+} ions during deep discharging when Ti content is high enough, which decreases the concentration of Jahn–Teller Mn^{3+} ions. However, some Mn^{2+} ions could occupy Li^+ at 8a sites during Ti substitution for Mn, which may lead to deteriorated rate capability. Therefore, the optimal content of Ti is needed to obtain

the best performance. In our case, the $\text{LiMn}_{1.5}\text{Ti}_{0.5}\text{O}_4$ electrode exhibits a high capacity, excellent cycling stability, and remarkable rate capability, making it attractive for electric vehicle applications.

Acknowledgments

Financial support from National Basic Research Program of China (973 program, Grant No. 2011CB935903) and National Natural Science Foundation of China (Grant No. 21233004 and 21021002) are gratefully acknowledged. *In situ* electrochemical XRD were performed at beamline BL14B1 at the Shanghai Synchrotron Radiation Facility (SSRF) (Shanghai, China). Work at the University of Washington is in part supported by the Kyocera Foundation.

Appendix A. Supplementary data

Supplementary data related to this article can be found at <http://dx.doi.org/10.1016/j.jpowsour.2013.07.021>.

References

- [1] J.M. Tarascon, E. Wang, F.K. Shokoohi, W.R. McKinnon, S. Colson, *J. Electrochem. Soc.* 138 (1991) 2859–2864.
- [2] S. Lee, Y. Cho, H.-K. Song, K.T. Lee, J. Cho, *Angew. Chem. Int. Ed.* 51 (2012) 8748–8752.
- [3] T.J. Richardson, P.N. Ross Jr., *Mater. Res. Bull.* 31 (1996) 935–941.
- [4] D. Peramunage, K.M. Abraham, *J. Electrochem. Soc.* 145 (1998) 1131–1136.
- [5] J. Feng, B. Song, M.O. Lai, L. Lu, X. Zeng, Z. Huang, *Funct. Mater. Lett.* 05 (2012) 1250028.
- [6] J.B. Goodenough, K.-S. Park, *J. Am. Chem. Soc.* 135 (2013) 1167–1176.
- [7] M.M. Thackeray, W.I.F. David, P.G. Bruce, J.B. Goodenough, *Mater. Res. Bull.* 18 (1983) 461–472.
- [8] J. Kim, A. Manthiram, *Electrochem. Solid-State Lett.* 1 (1998) 207–209.
- [9] D. Song, H. Ikuta, T. Uchida, M. Wakihara, *Solid State Ionics* 117 (1999) 151–156.
- [10] V.L. Chevrier, S.P. Ong, R. Armiento, M.K.Y. Chan, G. Ceder, *Phys. Rev. B* 82 (2010) 075122.
- [11] B. Xu, S. Meng, *J. Power Sources* 195 (2010) 4971–4976.
- [12] C.Y. Ouyang, S.Q. Shi, M.S. Lei, *J. Alloys Compd.* 474 (2009) 370–374.
- [13] Y. Gao, J.R. Dahn, *J. Electrochem. Soc.* 143 (1996) 100–114.
- [14] J.H. Kim, S.T. Myung, Y.K. Sun, *Electrochim. Acta* 49 (2004) 219–227.
- [15] M. Takahashi, T. Yoshida, A. Ichikawa, K. Kitoh, H. Katsukawa, Q. Zhang, M. Yoshio, *Electrochim. Acta* 51 (2006) 5508–5514.
- [16] Y.-S. Lee, M. Yoshio, *Electrochem. Solid-State Lett.* 4 (2001) A85–A88.
- [17] B. Ebin, S. Gürmen, C. Arslan, G. Lindbergh, *Electrochim. Acta* 76 (2012) 368–374.
- [18] L. Hernán, J. Morales, L. Sánchez, J. Santos, *Solid State Ionics* 118 (1999) 179–185.
- [19] Y.S. Lee, H.J. Lee, M. Yoshio, *Electrochem. Commun.* 3 (2001) 20–23.
- [20] E.-S. Lee, K.-W. Nam, E. Hu, A. Manthiram, *Chem. Mater.* 24 (2012) 3610–3620.
- [21] M. Lin, S.H. Wang, Z.L. Gong, X.K. Huang, Y. Yang, *J. Electrochem. Soc.* 160 (2013) A3036–A3040.
- [22] G. He, Y. Li, J. Li, Y. Yang, *Electrochem. Solid-State Lett.* 13 (2010) A19–A21.
- [23] D. Lv, J. Bai, P. Zhang, S. Wu, Y. Li, W. Wen, Z. Jiang, J. Mi, Z. Zhu, Y. Yang, *Chem. Mater.* 25 (2013) 2014–2020.
- [24] G. Kresse, J. Furthmüller, *Phys. Rev. B* 54 (1996) 11169–11186.
- [25] P.E. Blöchl, *Phys. Rev. B* 50 (1994) 17953–17979.
- [26] G. Kresse, D. Joubert, *Phys. Rev. B* 59 (1999) 1758–1775.
- [27] J.P. Perdew, K. Burke, M. Ernzerhof, *Phys. Rev. Lett.* 77 (1996) 3865–3868.
- [28] N. Krins, F. Hatert, K. Traina, L. Dusoulier, I. Molenberg, J.F. Fagnard, P. Vanderbemden, A. Rulmont, R. Cloots, B. Vertruyen, *Solid State Ionics* 177 (2006) 1033–1040.
- [29] K. Petrov, R.M. Rojas, P.J. Alonso, J.M. Amarilla, M.G. Lazarraga, J.M. Rojo, *Solid State Sci.* 7 (2005) 277–286.
- [30] G.T.-K. Fey, C.-Z. Lu, T.P. Kumar, *J. Power Sources* 115 (2003) 332–345.
- [31] L. Xiao, Y. Zhao, Y. Yang, Y. Cao, X. Ai, H. Yang, *Electrochim. Acta* 54 (2008) 545–550.
- [32] L. Xiong, Y. Xu, T. Tao, J.B. Goodenough, *J. Power Sources* 199 (2012) 214–219.
- [33] S. Suzuki, M. Tomita, S. Okada, H. Arai, *J. Phys. Chem. Solids* 57 (1996) 1851–1856.
- [34] J.-Y. Luo, H.-M. Xiong, Y.-Y. Xia, *J. Phys. Chem. C* 112 (2008) 12051–12057.
- [35] H. Berg, J.O. Thomas, W. Liu, G.C. Farrington, *Solid State Ionics* 112 (1998) 165–168.
- [36] J.-Y. Shin, D. Samuelis, J. Maier, *Adv. Funct. Mater.* 21 (2011) 3464–3472.
- [37] M.A. Arillo, G. Cuello, M.L. López, P. Martín, C. Pico, M.L. Veiga, *Solid State Sci.* 7 (2005) 25–32.
- [38] A. Du Pasquier, A. Blyr, P. Courjal, D. Larcher, G. Amatucci, B. Gérard, J.M. Tarascon, *J. Electrochem. Soc.* 146 (1999) 428–436.
- [39] K.Y. Chung, H.S. Lee, W.-S. Yoon, J. McBreen, X.-Q. Yang, *J. Electrochem. Soc.* 153 (2006) A774–A780.
- [40] X. Sun, X.Q. Yang, M. Balasubramanian, J. McBreen, Y. Xia, T. Sakai, *J. Electrochem. Soc.* 149 (2002) A842–A848.
- [41] Y. Xia, T. Sakai, T. Fujieda, X.Q. Yang, X. Sun, Z.F. Ma, J. McBreen, M. Yoshio, *J. Electrochem. Soc.* 148 (2001) A723–A729.
- [42] M. Nakayama, M. Nogami, *Solid State Commun.* 150 (2010) 1329–1333.